A climatology of surface–air temperature difference over the Tibetan Plateau: Results from multi-source reanalyses

Xuejia Wang [a, b], Deliang Chen [b], Guojin Pang [c, b], Tinghai Ou [b], Meixue Yang [a], Meng Wang [d]

a *State Key Laboratory of Cryosphere Science, Northwest Institute of Eco-Environment and Resources, Chinese Academy of Sciences, Lanzhou, Gansu 730000, China*

b *Regional Climate Group, Department of Earth Sciences, University of Gothenburg, Gothenburg 40530, Sweden*

c *Faculty of Geomatics, Lanzhou Jiaotong University, Lanzhou, Gansu 730070, China*

d *Forestry College, Southwest Forestry University, Kunming, Yunnan 650224, China*

**Corresponding authors*:
Xuejia Wang [1, 2] and Deliang Chen [2]
1. State Key Laboratory of Cryosphere Science, Northwest Institute of Eco-Environment and Resources, Chinese Academy of Sciences, Lanzhou, Gansu 730000, China
2. Regional Climate Group, Department of Earth Sciences, University of Gothenburg, Gothenburg 40530, Sweden Tel.: +46-31-7864813
E-mail: xjwang@lzb.ac.cn (X.Wang); deliang@gvc.gu.se (D. Chen)

Running head

Surface–air temperature difference over the Tibetan Plateau

This article has been accepted for publication and undergone full peer review but has not been through the copyediting, typesetting, pagination and proofreading process which may lead to differences between this version and the Version of Record. Please cite this article as doi: 10.1002/joc.6568

Abstract

The Tibetan Plateau (TP), known as Earth's "Third Pole", influences regional and even global weather and climate systems through its mechanical and thermal-dynamical forcing. Near-surface (2 m) air temperature (T_a) and surface (skin) temperature (T_s) are two crucial parameters of land-atmosphere interactions and climate change. Their difference ($\triangle T = T_s - T_a$) determines the heating source over the TP that drives the Asian summer monsoon. This study focuses on climatology, interannual variability, and long-term trend of $\triangle T$ over the TP in the last four decades (1979–2018), based on four latest reanalysis datasets including ERA-Interim, ERA5, MERRA2, and JRA55, along with observational data. We show that $\triangle T$ based different datasets display fairly different climatology in terms of seasonality, spatial distribution, and long-term trend. $\triangle T$ exhibits a clear seasonality with negative value in winter and positive ones in summer despite of different strengths and timings presented by the reanalyses. Along with global warming, all reanalyses except JRA55 exhibit obvious downward trends of $\triangle T$ in a spatially non-uniform way. The median $\triangle T$ among the four reanalyses features uniform decreases in all seasons, with the most distinct area on the northern TP as well as the largest and least decreases in autumn and spring, respectively. Further analysis shows that the differences in $\triangle T$ are most likely associated with discrepancies in radiation forcing, snow cover, wind speed, and boundary layer height within the reanalyses. The present findings highlight the difficulty for the state-of-the-art reanalyses to represent the climate change over the TP and point to possible factors behind the deficiencies identified.

Keywords: Tibetan Plateau; Air temperature; Surface temperature; Surface-air temperature difference; Reanalysis dataset

1. Introduction

There is a hydrologically and energetically coupled relationship between the land-surface and the lower atmosphere (Seneviratne et al., 2010; García-García et al., 2019). Changes of atmospheric variables directly alter land-surface status by means of changes in atmospheric circulation, air temperature, precipitation, winds, and clouds. Land-surface condition variations in terms of albedo, snow cover, soil moisture, and vegetation trigger the changes of surface energy partition and water balance, which finally exert impacts on atmospheric processes (e.g., Koster et al., 2004; Wang et al., 2016; Feng and Zou, 2019; Frick and Tervoore, 2019). Near-surface air temperature (T_a) and surface (skin) temperature (T_s) are both important parameters of the Earth's energy budget, land-atmosphere interactions, and climate change. T_a describes the kinetic energy of the near surface atmosphere and has a significant influence on evaporation, humidity, wind, and precipitation types. T_s is found to differ with T_a with respect to both physical meaning and magnitude (Jin and Dickinson, 2010; Rongali et al., 2018) and is controlled by downward terrestrial radiation, and therefore, by surface heat flux exchanges with the atmosphere. The land-atmosphere coupling is extremely complex and variable in both space and time, and its strength is often linked with extreme climate events such as heat weaves, droughts, and heavy rainfall, and so forth (Seneviratne et al., 2010; Zhang and Wu, 2011), which impact heavily on social life and economical activities.

The Tibetan Plateau (TP), often referred to as Earth's "Third Pole", is the world highest plateau with an average elevation of > 4000 m and an area of ~2.5×10^4 km^2 and exerts a considerable effect on regional and even global weather and climate systems through its mechanical and thermal-dynamical forcing (Wu et al., 2014). With global warming, T_a and T_s have increased obviously but with differing rates on the TP (Zhong et al., 2011) because of complex underlying surface turbulence and atmospheric motions. T_a and T_s are usually interdependent of and coupled to each other (Chen et al., 2016). They are complementary in their contribution of helpful knowledge to the study of climate change (Jin and Dickinson, 2010). The indicator of surface-air temperature difference (T_s–T_a, △T) is an exceedingly important variable that influences regional and even global climate and environment (Stull, 1998), as well as land-atmosphere interactions (Zhang et al., 2011). Previous studies have attempted to employ △T to conduct remote sensing retrieval of energy fluxes on the TP (Zhang et al., 2015) and to assess the capability of climate model (Koven et al., 2013). Compared with other regions at same Northern Hemisphere latitudinal zone, the TP acts as a huge heat source to the atmosphere (Duan and Wu, 2008; Yang et al., 2011), mainly through sensible heat flux (SHF). Driven by the heating, normally termed as sensible heat driven air-pump (Wu et al., 2012, 2014), the water vapor and air mass in the low-level atmosphere around the plateau are pumped to the TP during spring and summer. △T is also a direct and main contributor to SHF which plays a crucial role in the seasonal transition, onset, and maintenance of the Asian summer monsoon, affecting precipitation in China (Wu et al., 2014). Therefore, deep understanding of the spatial patterns and variations of △T over the TP is of great importance for elucidating their influence on SHF and heat source.

The entire TP has poor coverage of meteorological stations, most of which are concentrated on the central and eastern TP and low altitude areas (Yang et al., 2019). This makes it difficult and speculative to comprehend key processes crucial to regional climate and land-atmosphere interactions (Chen et al., 2015). Meanwhile, for routine T_s meteorological observation, China Meteorological Administration widely adopted automatic observation to replace previous manual observation after 2005. As the difference in criterion exists between the two methods, T_s recorded by automatic stations is generally higher in winter when snow cover exists than by manual observation (Liao et al., 2019). T_s is measured at the 0-cm level, mainly reflecting the bare land skin temperature, but the central and eastern TP is actually covered by vegetation (Zhu et al., 2012). Thus, there remains a large uncertainty in T_s from meteorological stations. And the observed △T do not reflect negative value and the well-known cold source over the TP during winter and may overestimate the summer heat source (Liao et al., 2019). This severely hampers our understanding of the regional △T change. These factors all motivate us to adopt alternative dataset which can provide much better geographic coverage and supporting climate variables.

Thereinto reanalysis products become increasingly acceptable and have been in vogue to be used by a greater number of scientists since it can best describe long-term and large-scale thermo-dynamical state of the atmosphere (Gao et al., 2019). By combining in-site observations and remote sensing data into an atmospheric model via data assimilation, model processes are constrained as much as possible to the real atmospheric state. This improved reliability enables attractive applications for reanalysis data in a series of scientific studies (Hinkelman, 2019). The prevalent reanalysis data with high-resolution performs well in reproducing the TP climate variables. For instance, MERRA has a high correlation with observations of surface meteorological variables (Wang and Zeng, 2012). ERA-Interim data shows relatively small cold bias in T_a (Wang et al., 2017) and better performance in water cycle (Wang and Zeng, 2012), as well as SHF on the TP (Chen et al., 2019).

Compared to the individual variable, either T_a or T_s, the spatial-temporal patterns of △T are more complicated (Feng and Zou, 2019). In recent years, numerous studies suggested that the SHF over the TP has undergone a weakening trend (e.g., Duan and Wu, 2008; Wang et al., 2013; Duan et al., 2018), which is attributed to the decreased surface wind speed (Duan and Wu, 2008). However, there has been relatively little systematic research on another important contributor △T over the TP, in particular, including its seasonality, interannual variability, and long-term trend. The objectives of this study are to identify these based on latest multi-source reanalysis datasets, and to further investigate possible causes for the discrepancies in △T among the reanalyses.

2. Data and evaluation strategy

2.1 Reanalysis datasets

Four reanalysis products containing T_s and 2-m T_a (hereafter referred to simply as T_a) are comprehensively used in the study (Table 1), since they are the latest generation and state-of the-art reanalyses. Monthly T_a and T_s are obtained from the Europe Centre for Medium-Range Weather Forecasting (ECMWF) ERA-Interim (hereafter ERAI) with a spatial resolution of ~ 79 km or ~ 0.75° for the period 1979-2018. The ERAI is an updated version of the ERA40 reanalysis and utilizes the data assimilation system of the Integrated Forecast System (Cy31r2). Besides, ERAI employs a 4-dimensional variational analysis (4D-Var) and has improved variational bias correction of satellite derived radiance data as well as humidity analyses and model physics (Dee et al., 2011).

Recently, ECMWF has developed its fifth-generation reanalysis product, namely ERA5 (the successor to ERAI) with a spatial resolution of ~ 31 km or ~ 0.25° (Hersbach et al., 2018). Relative to the former ERAI, substantial changes have been made for ERA5 in terms of higher temporal and spatial resolutions. ERA5 integrates ample amounts of reprocessed observations (satellite, ozone, aircraft, and surface pressure data) into global estimates using advanced Earth system model and data assimilation system of the IFS (Cy41r2).

In a reanalysis, a skin layer represents the vegetation layer, the top layer of the bare soil, or the top layer of the snow pack in its land surface model. T_s indicates the temperature at the interface between the land and atmosphere. In the ECMWF reanalysis family T_s is physically acquired from the surface-atmosphere energy balance of the land surface model, which connects the surface with the lowest atmospheric level through dry static energy, moisture and thermal contact with a single four-layer soil profile (or one layer if snow exists) (Dee et al., 2011).

Another reanalysis is the Modern-Era Retrospective analysis for Research and Applications, version 2 (MERRA2), which is released by the NASA Global Modeling and

Assimilation Office. MERRA2 has a native spatial resolution of 0.5° × 0.625° and is available from 1980 onwards. Modern hyperspectral radiance and microwave observations, as well as GPS-Radio Occultation datasets are incorporated into the NASA's Goddard Earth Observing System, version 5 (GEOS-5) via the GSI assimilation system (Gelaro et al., 2017). Thanks to these advances, many aspects in MERRA2 have been updated, including the representation of the cryosphere, T_a, and global mean radiative fluxes (Hinkelman, 2019). MEERA2 T_s is from the Catchment land surface model, a component of the GEOS-5, and assimilation system (Draper et al., 2018).

In addition, we also make use of the Japanese 55-year Reanalysis (JRA55; 1.25° × 1.25° grid) conducted by the Japan Meteorological Agency (Kobayashi et al., 2015). T_s is represented by the brightness temperature in JRA55, which is computed from surface upward longwave radiation assuming that surface acts as a black body. Similar to ERAI, JRA55 incorporates snow observations over the TP region.

To investigate the differences in ΔT variations among reanalyses, downward shortwave and longwave radiations (DSR and DLR), snow depth, wind speed at 10 m above ground level (WS), and boundary layer height (BLH) are extracted from the corresponding reanalysis datasets. Following Orsolini et al. (2019), snow depth is converted to snow cover fraction (SCF).

2.2 Observational datasets

Two sets of ancillary observational data of 2-m T_a are also utilized. Observational CN05.1 gridded data (hereafter CN05, a spatial resolution of 0.25° × 0.25°) covering the TP is used, which is interpolated based on 2416 stations in China (Wu and Gao, 2013). It has been widely used in the validation and evaluation of climate simulations and climate change (Guo et al., 2018; Wang et al., 2016, 2018). For comparison purpose, another monthly T_a data is obtained from the gridded observations CRU (Climate Research Union) with a spatial resolution of 0.5° × 0.5° produced by University of East Anglia (Mitchell and Jones, 2005). Likewise, the gridded temperatures are interpolated from quality-controlled meteorological station data based on a presumed correlation decay distance. Furthermore, we also resort to the monthly satellite land surface temperature (LST) data–that is MODIS/Terra MOD11C3 Collection 6 covering the time period from February 2000 to December 2018 at 0.05° spatial resolution (Wan et al., 2015)–as a reference data to manifest the performance of the reanalysis products in T_s.

2.3 Evaluation strategy

Since the time spans of these reanalysis datasets are somewhat different, this paper simply focuses on the common time period 1979-2018 (40 years) except for MERRA2 starting from 1980 and for CN05 and CRU being used until 2016 and 2017, respectively. Due to different spatial resolutions (Table 1), for the spatial distribution and trend of the median ΔT among the four reanalyses, we interpolate T_s and T_a into a common resolution of 1.5°×1.5° based on the bilinear interpolation method, although this may obscure some of the added value of high-resolution data and introduce some errors because of complex climate and underlying surfaces.

The performances of the four reanalysis datasets in T_a and T_s are evaluated prior to the ΔT analyzing. To examine the statistical difference of the two variables, significance test for the difference ΔT is implemented using the two-tailed Student's t test (Wilks, 2006). Linear regression trends based on the least-squares method are also applied for regional averaged winter (December–February, DJF), spring (March–May, MAM), summer (June–August, JJA), and autumn (September–November, SON) climate variables. The significance test for the linear trend is performed using the two-tailed Student's t test (Santer et al., 2000).

The median of the multi-reanalysis products is computed, which can reduce the influence by extremely large and small values (Wang et al., 2019). Relationships (r) between climate variables (DSR, DLR, SCF, WS, and BLH) and ΔT within the same reanalysis product are detected using the Pearson correlation analysis. We also use the seasonality and long-term trends of climate variables, together with the correlations to explain the differences in ΔT among the reanalyses.

3. Climatology of △T from multi-source reanalyses

3.1 Evaluation of Temperature (T_a and T_s)

We first compare climatological annual cycle of T_a from observations (CRU and CN05) and reanalyses (Figure 2). All reanalyses reproduce reasonably well the annual changes of T_a. T_a in ERAI is slightly higher than the observations, consistent with the result of Wang et al. (2017). Yet other three reanalyses have a negatively bias partly due to the fact that most of meteorological stations record warm temperature since they are concentrated in inhabited valleys.

Intercomparisons among the reanalyses show that ERA5 produces relatively cold temperatures, particularly in winter (Figure 2a, Table S1). Topography may play a vital influence on near-surface temperature. There are evident elevation differences among these reanalyses (Figure 1). A noted fact is that much finer resolution model can better depict topography and likely generates high terrain, leading to a cold temperature. Nevertheless, coarse resolution modeling generates relatively low and flat terrain, resulting in a warm temperature. Between the ECMWF family reanalyses, ERAI has a better performance in reproducing snow depth over the TP (Orsolini et al., 2019). It is due to the fact that snow cover from Interactive Multisensor Snow and Ice Mapping System (IMS) was considered by ERAI, even in high altitude regions, including the TP, whereas IMS data above 1500 m was not assimilated in the production of ERA5, resulting in overestimated SCF and days on the TP, nearly 3 times of observed data (Orsolini et al., 2019). Consequently, ERA5 most likely simulates much stronger albedo effect of snow, forming cold temperature. This feature is more obvious in cold season (Table S1). Compared with CN05, MERRA2 and JRA55 have small biases and RMSE, ERAI performs best in T_a except for DJF series.

When it comes to T_s, though appreciable differences exist, the annual change is consistently reproduced by the four reanalyses. Warmest T_s is produced by MERRA2 across the whole year (Figure 2b), coldest by JRA55 during summer, ERA5 still tends to yield cold T_s

with exception of summer when it shares nearly similar T_s with ERAI (Table S1). These differences may be attributable to numerous factors, such as diverse land surface schemes, atmospheric models, and observational data assimilating sources (Table 1). Land surface schemes which emphasize different land surface processes-such as vegetation, snow melting process, and soil water-heat transfer-simulate diversified partition of surface energy (Yang et al., 2009; Wang et al., 2014, 2016). Additionally, atmospheric models' resolution and physics design, together with the use of data assimilation system have large impacts on atmospheric circulations and surface energy and water budgets. In comparison with MODIS LST, all reanalysis data generate warmer T_s in JJA but colder ones in the rest of the seasons. JRA55 forms much closer T_s with MODIS data in DJF and JJA, while MERRA2 shows the best performance in MAM (Table S1). Considering above comparisons, no reanalysis clearly stands out as the best performing one for all seasons and variables, and each of the reanalyses displays different biases. It is highlighted that combined utilization of reanalysis data with various data sources is beneficial for understanding the TP ΔT changes.

3.2 Spatial-temporal distribution of ΔT

Figure 2c shows the climatological annual cycle of ΔT over the TP. Overall highest ΔT is attained by MERRA2, lowest ΔT by ERA5 during winter (reaching up to -3.7 °C) and spring and by ERAI during transitional seasons. Although there are some differences in the magnitudes of ΔT among the four reanalyses, the variations are basically consistent. However, the timing of the peak has a disagreement across the reanalyses. ΔT in MERRA2 and JRA55 peak in June, one month earlier than the ECMWF family of reanalyses. These may reflect inconsistencies in the activity and onset of summer monsoon among these reananlyses. The median of the four reanalyses shows that ΔT has strong seasonal variability, with maximum in JJA (1.7 °C) and minimum in DJF (-1.8 °C).

In terms of the spatial distribution (Figure 3), CN05 and all the reanalyses indicate that the TP has a large-scale negative T_a and ΔT in DJF, suggesting an obvious cold source over the TP in winter. From the ECMWF datasets, substantial negative ΔT occur over high mountains, such as the Karakorum Mountains, the Himalayas, the mountains in the southeastern TP, and the Qilian Mountains. More details are generated by ERA5 because of its higher resolution. Unlike the ECMWF reanalyses, MERRA2 produced large ΔT mainly appear along the Himalayas and in the Qilian Mountains. In spite of sharing approximately the similar spatial resolution, the result of ΔT between ERAI and MERRA2 is quite diverse. JRA55 shows large ΔT appearing on the northwestern TP. The median exhibits the strongest cold source (Figure 3f), as indicated by the most negative ΔT.

In MAM, T_a gradually increases, the spatial patterns of ∆T manifested by the four reanalyses are quite different. Positive ∆T in the ECMWF begin to appear over the western TP and the Qaidam basin, while negative ones still exist in the southeastern TP and the Himalayas with decreased strengths. MERRA2 shows entirely positive ∆T on the TP. As for JRA55, positive ∆T is located on most of the TP. The median resembles the spatial pattern of ECMWF reanalyses (Figure 3l), but the regional mean ∆T quickly turns into positive value (Table S2), signifying a shift to a heat source for the TP.

As T_a turns entirely positive in JJA, the four reanalyses reveal similar pattern with positive ΔT over the vast majority of the TP. Large ΔT are located in the western and northern TP, and some part in the southern TP. MERRA2 has totally positive ΔT and the largest value, while ERAI and JRA55 possess the same and smallest ΔT (Table S2). The median result indicates higher ΔT appears in the western TP than in the eastern TP, yet smallest ΔT in the southeastern TP where monsoon precipitation occurs frequently, reducing T_s and ΔT (Figure 3r). The median ΔT is the highest among four seasons, denoting the heat source reaches its greatest strength in JJA.

As solar radiation weakens (T_a decreases accordingly) and the monsoon withdraws, ΔT decreases rapidly from JJA to SON and then quickly transforms into negative values, with a regional averaged value of -0.3 °C. It means that the heat source reduces its strength.

Discrepancies of inter-reanalysis are appreciable, which is comparable to those in MAM. The median displays negative ΔT in the southeastern TP and positive value in the northwestern TP (Figure 3x).

3.3 Interannual variation of ΔT

Figure 4 shows the spatial distribution of seasonal trends in T_a and ΔT over the TP. CN05 reveals significant increasing trends in T_a in all four seasons, with highest in DJF and smallest in JJA. ΔT change varies spatially among these reanalyses. The two ECMWF reanalyses show a large area of decreasing trend in ∆T, most notably in the northeastern TP, while somewhat increasing trend appears in the western TP, the Himalayas, and the southeastern TP. Comparatively high decreasing trend is represented by ERAI, especially in DJF and SON. With exception of DJF, MERRA2 displays a spatial pattern marked by an increasing trend in the western TP but a decreasing trend in the eastern TP. Areas with negative and positive trends account for approximately half of the TP, respectively. On the contrary, JRA55 presents distinct increasing trends in ∆T particularly during DJF apart from the northern TP. Overall, ∆T in the median presents widespread downward trends across the four seasons with the most prominent area occurring in the northern TP, while somewhat upward trends are observed in the western and southeastern TP.

The time series of seasonal average ∆T for the whole TP from the reanalysis products exhibit marked discrepancies (Figure 5). The ECMWF reanalyses, especially ERAI, present significantly decreasing trends in ∆T. MERRA2 gives almost invariable trends in DJF and MAM but slightly decreasing trends in the remaining seasons. As to JRA55, there are significantly increasing trends, especially in DJF. Moreover, ∆T time series of the reanalyses exhibit large fluctuations in DJF and MAM, indicating large year-to-year variability. Similar decreasing trends are also reported by NCEP reanalysis data (Chen et al., 2019). Taken together, the median ∆T has decreased significantly in four seasons from 1979 to 2018 (Table S2), in accord with the decline of SHF (Wang et al., 2013; Duan et al., 2018) and the reduction of heating ability in recent decades (Yang et al., 2011). The largest decrease occurs in SON at a rate of 0.045 °C decade $^{-1}$, while the least decrease appears in MAM at a rate of 0.037 °C decade $^{-1}$.

4. Why ΔT are different in the reanalyses?

Several complex interactions for the TP rapid warming have been detected in recent decades. For instance, the TP warming is due to CO2 increase (Chen et al., 2003). Locally, radiation balance caused by snow albedo feedback imposes great impacts on T_a and T_s (e.g., Chen et al., 2017; Gao et al., 2019; Guo et al., 2020). WS decline lessens the Bowen ratio and generates less surface sensible heating, accounting for the TP warming (Yang et al., 2014). In this section, downward radiation forcing, SCF, WS, and BLH are used here to investigate the causes of the differences in △T among the reanalyses.

4.1 Downward radiation forcing

Radiation forcing (DSR and DLR) are expected to have dominant influences on △T as they are the control factors of temperature. Figure 6a shows scatterplot of downward radiations versus △T. Both DSR and DLR have significantly positive correlations with △T. This indicates that strong downward radiation forcing tend to generate a positive △T, vice versa. Furthermore, DLR has a larger impact on △T than DSR in terms of higher correlation coefficient except for MERRA2, mainly because there is similar seasonal evolution between DLR and △T, i.e. highest in JJA and lowest in DJF (Figure 6d). MERRA2 has stronger DSR and reaches its peak in June, which can impose great influence on △T, such as large positive △T and advanced peak time. Over time, DSR has a significant decreasing trend and DLR has an increasing trend in JJA, the increases of DLR in the reanalyses except for JRA55 are weaker than the decreases of DSR (Table 2), thus causing the decreases in △T. However, it is exactly the opposite for JRA55. In DJF and MAM, DSR and DLR display slightly positive trends over the past 40 years but exert complicated influences on △T because of their intensities and snow cover.

4.2 Snow cover

A prior study suggested that the albedo effect is governed by SCF (Xu and Dirmeyer, 2012). To examine the effect of snow cover on △T, we plot the correlation map between SCF and △T over the TP on monthly time scale (Figure 7a). There are negative correlations between monthly SCF and △T. It means large (small) SCF appears to yield negative (positive) △T. Climatologically, the large △T generally occur at high altitudes where large SCF appear (Figure 7b). During cold season, high snow cover tends to reflect solar radiation, leading to a lower T_s and a more negative △T, and vice versa. Among the four reanalyses, ERA5 generates the highest SCF over the TP, followed by JRA55, ERAI, and then MERRA2, in accord with the result of Orsolini et al. (2019). That helps to explain ERA5 has large negative ΔT in DJF and MAM. In the case of MERRA2, the smallest SCF is more likely to lead to less negative ΔT, and the rapid response of ΔT to SCF is partly the cause for ΔT's dramatic transition from negative in DJF to positive in MAM. For JRA55, the response of △T to SCF is slow from snow season to snow free season (JJA).

Snow cover has been reported to have reduced over the past decades (Yang et al., 2019), characterized by greater decreasing magnitudes in DJF and MAM than in JJA (Table 2). High elevation warming is ascribed to snow cove/ice-albedo feedback. Accordingly, some increases of ΔT in high-elevation areas revealed by ECMWF reanalyses are likely associated with the decrease of SCF in DJF and MAM. For JRA55, notably reduced SCF in DJF together with increased radiation forcing act to cause a large increase in △T. Large year-to-year variability of the snow cover among the reanalyses may contribute to the great diversity of △T.

4.3 Wind speed (WS)

WS is a dynamic factor affecting the exchange of turbulent heat fluxes. Since WS can affect land surface energy balance through evapotranspiration and surface heat flux, and WS change is constrained by processes that have a scale beyond the atmospheric boundary layer (Yang et al., 2014). WS also exhibits a strengthening-weakening seasonal variation from DJF to SON, with a maximum value in MAM (Figure 8b), meaning that the peak time of WS is ahead of △T. Among the reanalyses, MERRA2 has the largest WS, while JRA55 has the smallest WS. At the monthly scale, negative correlations suggest that high WS is likely to produce small △T (Figures 8a). In terms of WS change, the reanalyses reach a consistent result that shows increases in JJA and SON, which are in agreement with the decreases of △T. Between the ECMWF reanalyses, having nearly similar variation tendencies of DSR and DLR in SON, the decreases of △T are very different, partly due to the obvious difference of WS variation (Table 2).

4.4 Boundary layer height (BLH)

The development of planetary boundary layer is strongly relevant to convection activity and complex surface forcing containing SHF, frictional drag, evapotranspiration, and terrain-induced flow modification (Stull, 1988). The effective heat capacity, resolved by the air column with mixed heat, influences T_a to some degree. This heat is determined by a surface heat flux and runs through the PBL. The shallower BLH, the lower effective heat capacity and the more sensitive T_a is to forcing (Esau et al., 2012). BLH is missing in JRA55, thus the correlations are calculated using the other three reanalysis products (Figure 9a). Positive correlations between monthly BLH and ΔT imply large BLH results in positive ΔT. The largest ΔT is generated by MERRA2 in JJA and the smallest by ERA5 in DJF (Figure 9b), corresponding to their respective largest BLH and smallest BLH. A strongly amplified temperature response can be obtained in shallow boundary layers (Davy and Esau, 2016). In a warming climate, obvious decreasing trends in BLH are found in ERAI in the four seasons, which amplifies T_a warming response and causes the decreases of △T. In JJA, BLH have reduced significantly in all reanalyses, contributing to the △T decreases (Table 2).

5. Summary and discussion

The study utilizes T_s and T_a data from four recent and state-of-the-art reanalysis datasets (ERAI, ERA5, MERRA2, and JRA55) to reveal spatiotemporal variability of △T over the TP from 1979 to 2018. The TP ΔT exhibits a strong seasonal cycle with negative value in DJF and positive value in JJA, suggesting the seasonal transition from heat sink to heat source. However, there are significant differences in terms of peak time and strength of ΔT among the reanalyses. Under climate warming, apart from JRA55, the reanalyses present decreasing trends of ΔT in a spatially non-uniform way over the studied period. Generally, the median of the four reanalyses exhibits significantly negative trends across four seasons with the most pronounced area in the northern TP and the largest decrease in SON as well as the least decrease in MAM. The decreases in ΔT during DJF and SON suggest the strength of the TP cold sources have enhanced and increased near-surface temperature inversion have suppressed air convection and mixing. These results of decreasing ΔT are in favor of the decline of SHF, implying that the TP heat sources in MAM and JJA have reduced their strength, which may exert significant influences on the monsoon onset and intensity.

The differences in the spatiotemporal variability of ΔT among the reanalyses are relevant with radiation forcing, SCF, WS, and BLH at different intensities and time scales (mainly seasonality and interannual variability). Overall, ΔT is positively correlated to DSR and DLR as well as BLH, but negatively correlated to SCF and WS. Additionally, other causes, such as precipitation, vegetation condition, and soil moisture may also play important roles. T_s is response to wetting and drying cycles of soil, which are heavily modulated by precipitation. The vegetation is normally denser in wetter region. The vegetation types and their description in the reanalyses are remarkably different (Xie et al., 2019). ERA5 and MERRA2 adopt seasonally varying vegetation index to represent vegetation dynamics, but do not allow vegetation to change annually. Moreover, the existing reanalyses do not depict vegetation changes explicitly in the TP. These aspects should be kept in mind in future research.

Given high heterogeneity among reanalysis products covering the climatology of ΔT at the seasonal and interannual time-scales, using the reanalyses to represent climate change is not yet mature and should be refined in the future. Meanwhile, the different usage of data in assimilation system such as snow data in the ECMWF reanalyses, and the diverse physical parameterizations, i.e. land surface and boundary layer schemes, allow highlighting the importance of incorporating more satellite data and station observations into assimilation system and optimizing model parameterizations. Although interrelationships between influencing factors and ΔT are performed based on the identical reanalysis source to alleviate errors from different datasets, inherent biases are still inevitable. Therefore, a quality-controlled database containing various variables corresponding to T_s and T_a should be generated in future research to verify the results and further explore their difference and coupling. What's more, regional climate models-based research is required to enhance understanding of the regional details, as topographic features and their crucial effects on regional climate are not well resolved in coarse-resolution GCMs/reanalyses (Gao and Chen, 2017; Giorgi, 2019), as well as to estimate the impacts of dynamic vegetation and soil moisture.

Acknowledgements

This study is jointly supported by the Strategic Priority Research Program of the Chinese Academy of Sciences (CAS) (XDA20100102, XDA19070204), the Innovation Research Group of NSFC (41721091), the National Natural Science Foundation of China (41601077, 41571066, and 41771068), the CAS "Light of West China" Program, the Youth Innovation Promotion Association CAS (2018460), the Program of China Scholarship Council (201804910129), and the Second Tibetan Plateau Scientific Expedition and Research Program (STEP) (2019QZKK0208). This work is a contribution to the Swedish BECC and MERGE. The computations were performed on resources provided by the Swedish National Infrastructure for Computing (SNIC) at the National Supercomputer Centre in Sweden (NSC).

Reference

Chen B, Chao WC, Liu X. 2003. Enhanced climatic warming in the Tibetan Plateau due to doubling CO2: a model study. *Climate Dynamics*, 20(4): 401-413.

Chen D, Xu B, Yao T, Guo Z, Cui P, Chen F, Zhang R, Zhang X, Zhang Y, Fan J. 2015. Assessment of past, present and future environmental changes on the Tibetan Plateau. *Chinese Science Bulletin*, 60(32): 3025-3035.

Chen D, Tian Y, Yao T, Ou T. 2016. Satellite measurements reveal strong anisotropy in spatial coherence of climate variations over the Tibet Plateau. *Scientific Reports*, 6: 30304.

Chen L, Pryor SC, Wang H, Zhang R. 2019. Distribution and variation of the surface sensible heat flux over the central and eastern Tibetan Plateau: Comparison of station observations and multi‐reanalysis products. *Journal of Geophysical Research: Atmospheres*, 124: 6191-6206.

Chen X, Long D, Hong Y, Liang S, Hou A. 2017. Observed radiative cooling over the Tibetan Plateau for the past three decades driven by snow cover-induced surface albedo anomaly. *Journal of Geophysical Research: Atmospheres*, 122(12): 6170-6185.

Davy R, Esau I. 2016. Differences in the efficacy of climate forcings explained by variations in atmospheric boundary layer depth. *Nature Communications*, 7:11690.

Dee DP, Uppala SM, Simmons A *et al.* 2011. The ERA‐Interim reanalysis: Configuration and performance of the data assimilation system. *Quarterly Journal of the Royal Meteorological Society*, 137(656) :553-597.

Draper CS, Reichle RH, Koster RD. 2018. Assessment of MERRA-2 land surface energy flux estimates. *Journal of Climate*, 31(2): 671-691.

Duan A, Wu G. 2008. Weakening trend in the atmospheric heat source over the Tibetan Plateau during recent decades. Part I: Observations. *Journal of Climate*, 21(13): 3149-3164.

Duan A, Liu S, Zhao Y, Gao K, Hu W. 2018. Atmospheric heat source/sink dataset over the Tibetan Plateau based on satellite and routine meteorological observations. *Big Earth Data*, 2(2): 179-189.

Esau I, Davy R, Outten S. 2012. Complementary explanation of temperature response in the lower atmosphere. *Environmental Research Letters*, 7(4): 044026.

Feng H, Zou B. 2019. A greening world enhances the surface-air temperature difference. *Science of the Total Environment*, 658: 385-394.

Frick A, Tervooren S. 2019. A Framework for the Long-term Monitoring of Urban Green Volume Based on Multi-temporal and Multi-sensoral Remote Sensing Data. *Journal of Geovisualization and Spatial Analysis*, 3(1): 6.

Gao Y, Chen D (2017) Modeling of regional climate over the Tibetan Plateau. *Oxford Research Encyclopedia of Climate Science*. Doi: 10.1093/acrefore/9780190228620.013.591.

Gao K, Duan A, Chen D, Wu G. 2019. Surface energy budget diagnosis reveals possible mechanism for the different warming rate among Earth’s three poles in recent decades. *Science Bulletin*, 64(16): 1140-1143.

García-García A, Cuesta-Valero FJ, Beltrami H, Smerdon JE. 2019. Characterization of Air and Ground Temperature Relationships within the CMIP5 Historical and Future Climate Simulations. *Journal of Geophysical Research: Atmospheres*, 124: 3903–3929.

Gelaro R, McCarty W, Suárez MJ Todling, R., Molod, A., Takacs, L., Randles, C.A., Darmenov, A., Bosilovich, M.G., Reichle, R., Wargan, K., Coy, L., Cullather, R., Draper, C., Akella, S., Buchard, V., Conaty, A., Silva, A.M.d., Gu, W., Kim, G.-K., Koster, R., Lucchesi, R., Merkova, D., Nielsen, J.E., Partyka, G., Pawson, S., Putman, W., Rienecker, M., Schubert, S.D., Sienkiewicz, M. and Zhao, B. 2017. The modern-era retrospective analysis for research and applications, version 2 (MERRA-2). *Journal of Climate*, 30(14): 5419-5454.

Giorgi F. 2019. Thirty years of regional climate modeling: Where are we and where are we going next? *Journal of Geophysical Research: Atmospheres*, 124(11): 5696-5723.

Guo D, Sun J, Yu E. 2018. Evaluation of CORDEX regional climate models in simulating temperature and precipitation over the Tibetan Plateau. *Atmospheric and Oceanic Science Letters,* 11(3): 219-227.

Guo D, Sun J, Yang K, Pepin N, Xu Y, Xu Z, Wang H. 2020. Satellite data reveal southwestern Tibetan plateau cooling since 2001 due to snow-albedo feedback. *International Journal of Climatology,* 40(3): 1644-1655.

Hinkelman LM. 2019. The Global Radiative Energy Budget in MERRA and MERRA-2: Evaluation with Respect to CERES EBAF Data. *Journal of Climate,* 32(6):1973-1994.

Hersbach H, de Rosnay P, Bell B *et al.* 2018. Operational global reanalysis: progress, future directions and synergies with NWP, ECMWF ERA report series, N27. December 2018 (https://www.ecmwf.int/en/elibrary/18765-operational-global-reanalysis-progress-future-directions-and-synergies-nwp)

Jin M, Dickinson RE. 2010. Land surface skin temperature climatology: benefitting from the strengths of satellite observations. *Environmental Research Letters*, 5(4): 044004.

Kobayashi S, Ota Y, Harada Y *et al.* 2015. The JRA-55 reanalysis: General specifications and basic characteristics. *Journal of the Meteorological Society of Japan. Ser. II* 93(1): 5-48.

Koster RD, Dirmeyer PA, Guo Z *et al.* 2004. Regions of strong coupling between soil moisture and precipitation. *Science*, 305(5687): 1138-1140.

Koven CD, Riley WJ, Stern A. 2013. Analysis of permafrost thermal dynamics and response to climate change in the CMIP5 Earth System Models. *Journal of Climate*, 26(6) :1877-1900.

Liao Y, Chen D, Liu Q. 2019. The spatiotemporal characteristics and long-term trends of surface-air temperatures difference in China. *Advances in Climate Change Research*, doi:10.12006/j.issn.1673-1719.2018.199 (In Chinese with English Abstract).

Mitchell TD, Jones PD. 2005. An improved method of constructing a database of monthly climate observations and associated high - resolution grids. *International Journal of Climatology*, 25(6): 693-712.

Orsolini Y, Wegmann M, Dutra E, Liu B, Balsamo G, Yang K, de Rosnay P, Zhu C, Wang W, Senan R. 2019. Evaluation of snow depth and snow-cover over the Tibetan Plateau in global reanalyses using in-situ and satellite remote sensing observations. The Cryosphere, 13: 2221-2239.

Rienecker MM, Suarez MJ, Gelaro R, Todling R, Bacmeister J, Liu E, Bosilovich MG, Schubert SD, Takacs L, Kim G-K. 2011. MERRA: NASA’s modern-era retrospective analysis for research and applications. Journal of Climate, 24(14): 3624-3648.

Rongali G, Keshari A K, Gosain A K, et al. 2018. Split-window algorithm for retrieval of land surface temperature using Landsat 8 thermal infrared data. *Journal of Geovisualization and Spatial Analysis*, 2:14.

Santer BD, Wigley TML, Boyle JS, Gaffen DJ, Hnilo JJ, Nychka D, Parker DE, Taylor KE. 2000. Statistical significance of trends and trend differences in layer-average atmospheric temperature time series. *Journal of Geophysical Research: Atmospheres,* 105(D6): 7337-7356.

Seneviratne SI, Corti T, Davin EL, Hirschi M, Jaeger EB, Lehner I, Orlowsky B, Teuling AJ. 2010. Investigating soil moisture–climate interactions in a changing climate: a review. *Earth-Science Reviews,* 99(3): 125-161.

Stull RB. 1998. An introduction to boundary layer meteorology, Vol 13. Springer Science & Business Media.

Wan, Z., Hook, S., Hulley, G. 2015. MOD11C3 MODIS/Terra Land Surface Temperature/Emissivity Monthly L3 Global 0.05Deg CMG V006 [Data set]. NASA EOSDIS Land Processes DAAC. doi: 10.5067/MODIS/MOD11C3.006

Wang A, Zeng X. 2012. Evaluation of multireanalysis products with in situ observations over the Tibetan Plateau. *Journal of Geophysical Research*, 117(D5): D05102.

Wang M, Wang J, Chen D, Duan A, Liu Y, Zhou S, Guo D, Wang H, Ju W. 2019. Recent recovery of the boreal spring sensible heating over the Tibetan Plateau will continue in CMIP6 future projections. *Environmental Research Letters*,14: 124066.

Wang X, Yang M, Wan G. 2013. Temporal-spatial distribution and evolution of surface sensible heat flux over Qinghai-Xizang Plateau during last 60 years. *Plateau Meteorology,* 32(6): 1557-1567 (In Chinese with English Abstract).

Wang X, Yang M, Pang G. 2014. Sensitivity of regional climate simulations to land-surface schemes on the Tibetan Plateau. *Climate Research* 62(1): 25-43.

Wang X, Pang G, Yang M, Wan G. 2016. Effects of modified soil water - heat physics on RegCM4 simulations of climate over the Tibetan Plateau. *Journal of Geophysical Research: Atmospheres* 121(12): 6692-6712.

Wang X, Pang G, Yang M, Zhao G. 2017. Evaluation of climate on the Tibetan Plateau using ERA-Interim reanalysis and gridded observations during the period 1979–2012. *Quaternary International* 444: 76-86.

Wang X, Pang G, Yang M. 2018. Precipitation over the Tibetan Plateau during recent decades: a review based on observations and simulations. *International Journal of Climatology,* 38(3): 1116-1131.

Wilks DS. 2006. *Statistical methods in the atmospheric sciences.* Academic Press: San Diego, CA, 627 pp.

Wu G, Liu Y, He B, Bao Q, Duan A, Jin F-F. 2012. Thermal Controls on the Asian Summer Monsoon. *Scientific Reports* 2: 404.

Wu G, Duan A, Liu Y, Mao J, Ren R, Bao Q, He B, Liu B, Hu W. 2014. Tibetan Plateau climate dynamics: recent research progress and outlook. *National Science Review*, 2(1): 100-116.

Wu J, Gao X. 2013. A gridded daily observation dataset over China and comparison with the other dataset. Chinese Journal of Geophysics, 56(04): 1102-1111 (In Chinese with English Abstract).

Xie J, Yu Y, Li J, Ge J, Liu C. 2019. Comparison of surface sensible and latent heat fluxes over the Tibetan Plateau from reanalysis and observations. *Meteorology and Atmospheric Physics,* 131(3): 567-584.

Xu L, Dirmeyer P. 2012. Snow–atmosphere coupling strength. Part II: Albedo effect versus hydrological effect. *Journal of Hydrometeorology* 14(2): 404-418.

Yang K, Chen Y-Y, Qin J. 2009. Some practical notes on the land surface modeling in the Tibetan Plateau. *Hydrology and Earth System Sciences* 13(5): 687-701.

Yang K, Guo X, Wu B. 2011. Recent trends in surface sensible heat flux on the Tibetan Plateau. *Science China Earth Sciences* 54(1): 19-28.

Yang K, Wu H, Qin J, Lin C, Tang W, Chen Y. 2014. Recent climate changes over the Tibetan Plateau and their impacts on energy and water cycle: A review. *Global and Planetary Change,* 112: 79-91.

Yang M, Wang X, Pang G, Wan G, Liu Z. 2019. The Tibetan Plateau cryosphere: Observations and model simulations for current status and recent changes. *Earth-Science Reviews* 190: 353-369.

Zhang J, Gao S, Chen H, Yu J, Tang Q. 2015. Retrieval of the land surface - air temperature difference from high spatial resolution satellite observations over complex surfaces in the Tibetan Plateau. *Journal of Geophysical Research: Atmospheres* 120(16): 8065-8079.

Zhang J, Wu L. 2011. Land-atmosphere coupling amplifies hot extremes over China. *Chinese Science Bulletin* 56(31): 3328.

Zhang Q, Zhang J, Qiao J, Wang S. 2011. Relationship of atmospheric boundary layer depth with thermodynamic processes at the land surface in arid regions of China. *Science China Earth Sciences* 54(10): 158

Zhong L, Su Z, Ma Y, Salama MS, Sobrino JA. 2011. Accelerated changes of environmental conditions on the Tibetan Plateau caused by climate change. *Journal of Climate* 24(24): 6540-6550.

Zhu X, Liu Y, Wu G. 2012. An assessment of summer sensible heat flux on the Tibetan Plateau from eight data sets. *Science China Earth Sciences,* 55(5): 779-786.

Zhu L, Huang G, Fan G, Qü X, Wang Z, Hua W. 2019. Elevation-dependent sensible heat flux trend over the Tibetan Plateau and its possible causes. *Climate Dynamics* 52(7-8): 3997-4009.

Figure caption

Figure 1 Topography (m) of the TP described by the four reanalyses. The elevations of the longitudinal average over 72°E-106°E are shown to the right of each map.

Figure 2 Climatological annual cycles of air (T_a) and surface (skin) temperature (T_s) and their differences ($\Delta T= T_s-T_a$) during the period 1979-2018 for all data sets utilized, except for MODIS data which spans from 2002 to 2018. The dark green line in Figure 1c shows the median of the four reanalyses. The shading area indicates the 25^{th}-75^{th} percentile ranges in the multi-reanalyses.

Figure 3 Spatial distribution of seasonal mean air temperature (T_a, °C) from CN05 and surface-air temperature difference (ΔT, °C) over the TP between 1979 and 2018 revealed by ERAI, ERA5, MERRA2, JRA55, and the median of the four reanalyses. The dotted areas indicate ΔT exceeding the 95% confidence level.

Figure 4 Spatial distribution of seasonal trends (°C decade^{-1}) in T_a from CN05 and ΔT from ERAI, ERA5, MERRA2, JRA55, and the median among the four reanalyses on the TP during 1979 and 2018. The dots denote the trends exceeding the 95% confidence level.

Figure 5 Anomalies of temperature difference (ΔT) in four seasons of the four reanalyses and their median. The black dash line indicates linear regression of median. The shading area indicates the areas between 25% and 75% percentiles. The trends in T_a from CN05 and ΔT from the four reanalyses are labeled in each panel. * and ** indicate the trends exceeding the 95% and 99% confidence level, respectively.

Figure 6 Relationship between monthly ΔT and downward shortwave radiation (DSR), downward longwave radiation (DLR) from four reanalysis data sets and averaged annual cycles of DSR and DLR on the TP. ** indicates the correlation coefficients exceeding the 95% confidence level, respectively.

Figure 7 As Figure 6, but for snow cover fraction (SCF).

Figure 8 As Figure 6, but for 10-m wind speed (WS).

Figure 9 As Figure 6, but for boundary layer height (BLH). BLH is not available in JRA55.

Table 1 Information of datasets used in the study. E: elevation; DSR: downward shortwave radiation; DLR: downward longwave radiation; SD: snow depth; BLH: boundary layer height, WS: 10-m wind speed

Spatial resolution	Variables	Atmospheric model	Land surface model	Time span	Reference
0.25°	T_a	-	-	1961.01-2017.6	Wu and Gao,
0.5°	T_a	-	-	1901.01-2017.12	Mitchell and
0.05°	T_s	-	-	2000.02-2018.12	Wan et al., 20
0.75°	T_a, T_s, E, DSR, DLR, SD, WS, BLH	IFS Cy31r2	TESSEL	1979.01-2019.08	Dee et al., 20
0.25°	T_a, T_s, E, DSR, DLR, SD, WS, BLH	IFS Cy41r2	H-TESSEL	1979.01-present	Hersbach et a
0.5° × 0.625°	T_a, T_s, E, DSR, DLR, SD, WS, BLH	GEOS 5.12.4	Catchment LSM	1980.01-present	Gelaro et al.,
1.25°	T_a, T_s, E, DSR, DLR, SD, WS	JMA GSM	SIB	1958.01-present	Kobayashi et

Table 2 Trends of seasonal DSR (W m^{-2} $decade^{-1}$), DLR (W m^{-2} $decade^{-1}$), SCF ($decade^{-1}$), WS (m s^{-1} $decade^{-1}$), and BLH (m $decade^{-1}$) on the TP. * denotes the trend passes the significance level of 0.05.

Season	Variable	ERAI	ERA5	MERRA2	JRA55
DJF	DSR	0.58*	0.43*	0.40	0.02
	DLR	0.40	0.75*	0.91*	2.26*
	SCF	-0.010*	-0.014	-0.001	-0.037*
	WS	-0.01	-0.02*	-0.03*	0.00
	BLH	-4.57	10.85	9.00	
MAM	DSR	-0.03	-0.48	-1.57*	-0.81*
	DLR	0.65	0.88*	1.60*	1.54*
	SCF	-0.008*	-0.016*	-0.001	-0.001
	WS	-0.02	-0.03	-0.10*	-0.05
	BLH	-5.03	0.26	-0.85	
JJA	DSR	-3.11*	-2.53*	-3.40*	-3.65*
	DLR	2.39*	2.42*	3.32*	4.04*
	SCF	-0.002	-0.006*	0.000	0.001
	WS	0.04	0.02	0.02	0.02
	BLH	-15.60*	-7.13*	-12.31*	
SON	DSR	-0.51	-0.54	-0.73	-0.80*
	DLR	1.37*	1.43*	2.08*	1.51*
	SCF	0.000	-0.009	0.000	-0.013
	WS	0.03*	0.00	0.02	0.02
	BLH	-6.09	3.04	1.58	

DSR: downward shortwave radiation; DLR: downward longwave radiation; SCF: snow cover fraction; WS: wind speed; BLH: boundary layer height.

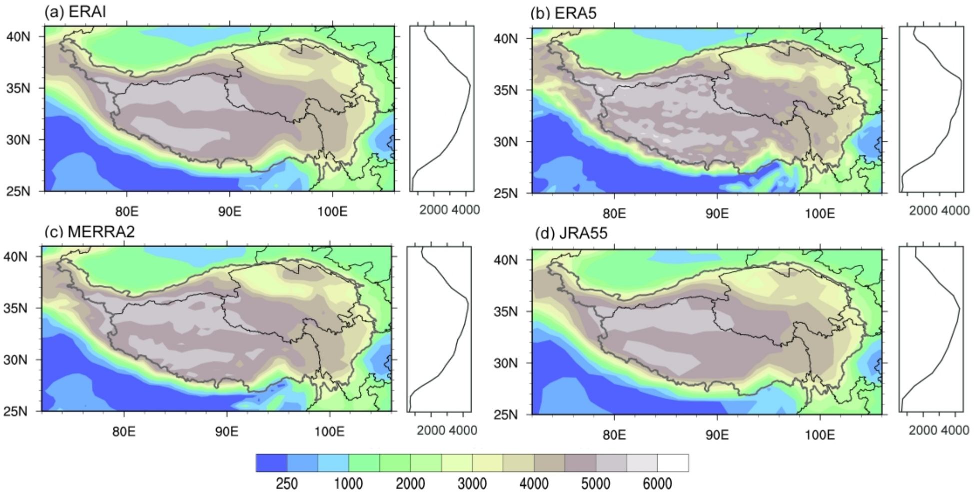

Figure 1 Topography (m) of the TP described by the four reanalyses. The elevations of the longitudinal average over 72°E-106°E are shown to the right of each map.

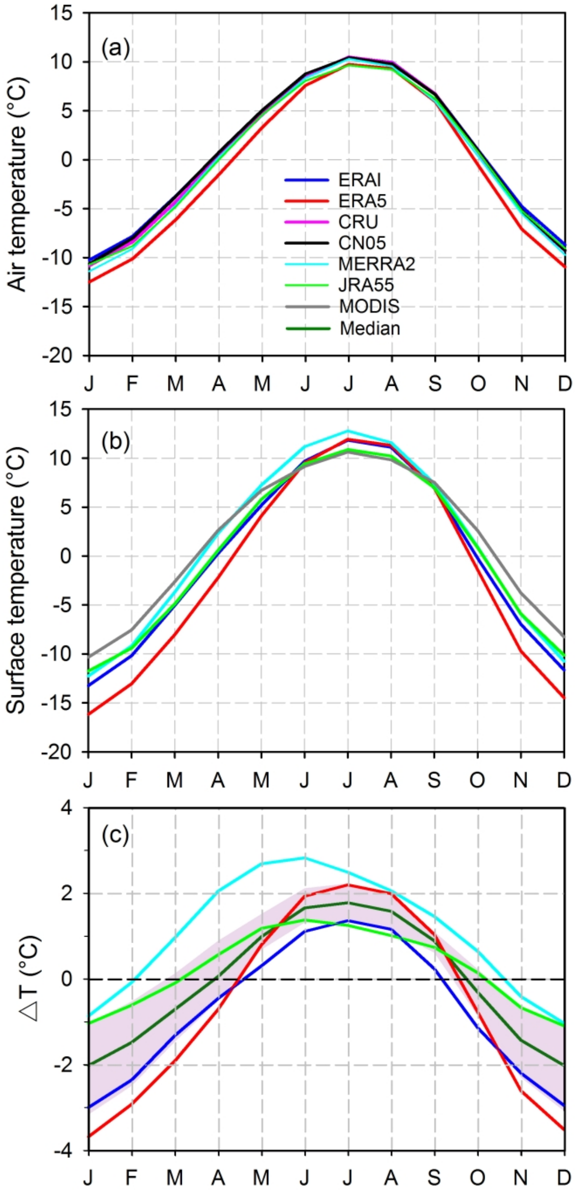

Figure 2 Climatological annual cycles of air (Ta) and surface (skin) temperature (Ts) and their differences (ΔT= Ts-Ta) during the period 1979-2018 for all data sets utilized, except for MODIS data which spans from 2002 to 2018. The dark green line in Figure 1c shows the median of the four reanalyses. The shading area indicates the 25th-75th percentile ranges in the multi-reanalyses.

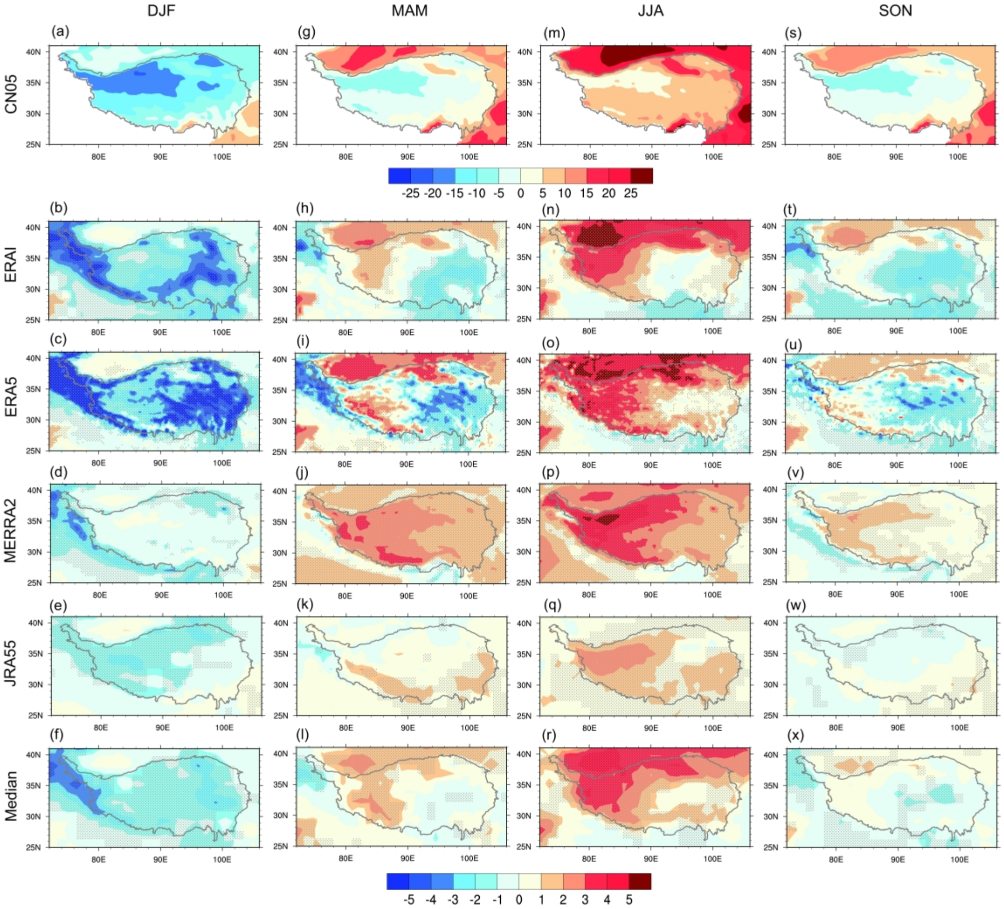

Figure 3 Spatial distribution of seasonal mean air temperature (Ta, °C) from CN05 and surface-air temperature difference (ΔT, °C) over the TP between 1979 and 2018 revealed by ERAI, ERA5, MERRA2, JRA55, and the median of the four reanalyses. The dotted areas indicate ΔT exceeding the 95% confidence level.

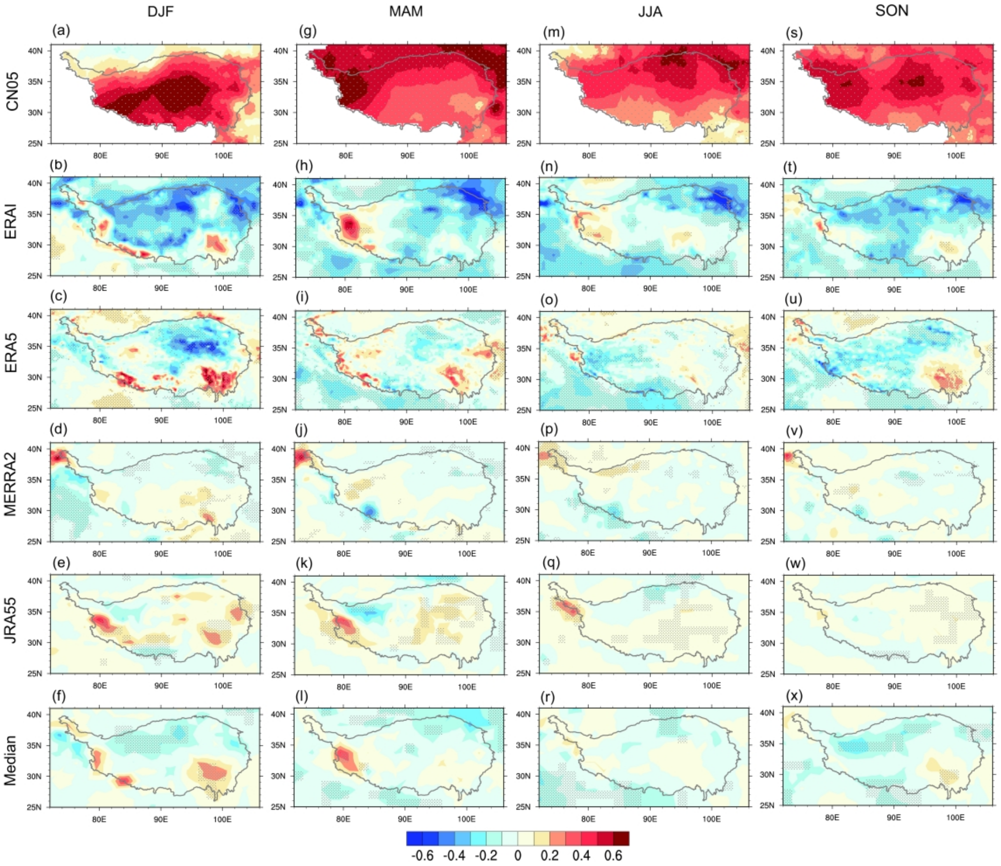

Figure 4 Spatial distribution of seasonal trends (°C decade-1) in Ta from CN05 and ΔT from ERAI, ERA5, MERRA2, JRA55, and the median among the four reanalyses on the TP during 1979 and 2018. The dots denote the trends exceeding the 95% confidence level.

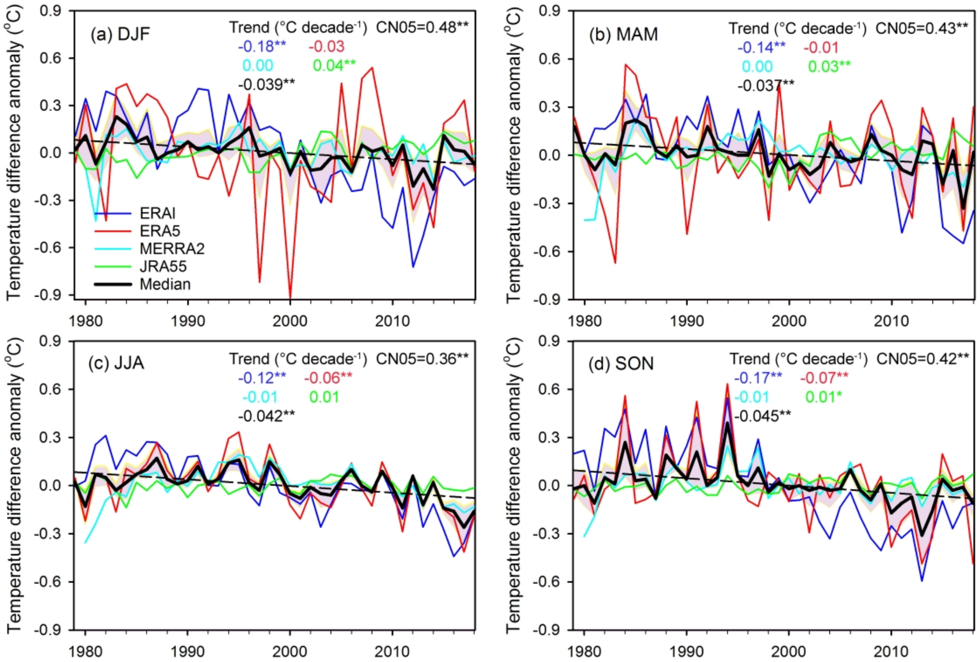

Figure 5 Anomalies of temperature difference (ΔT) in four seasons of the four reanalyses and their median. The black dash line indicates linear regression of median. The shading area indicates the areas between 25% and 75% percentiles. The trends in Ta from CN05 and ΔT from the four reanalyses are labeled in each panel. * and ** indicate the trends exceeding the 95% and 99% confidence level, respectively.

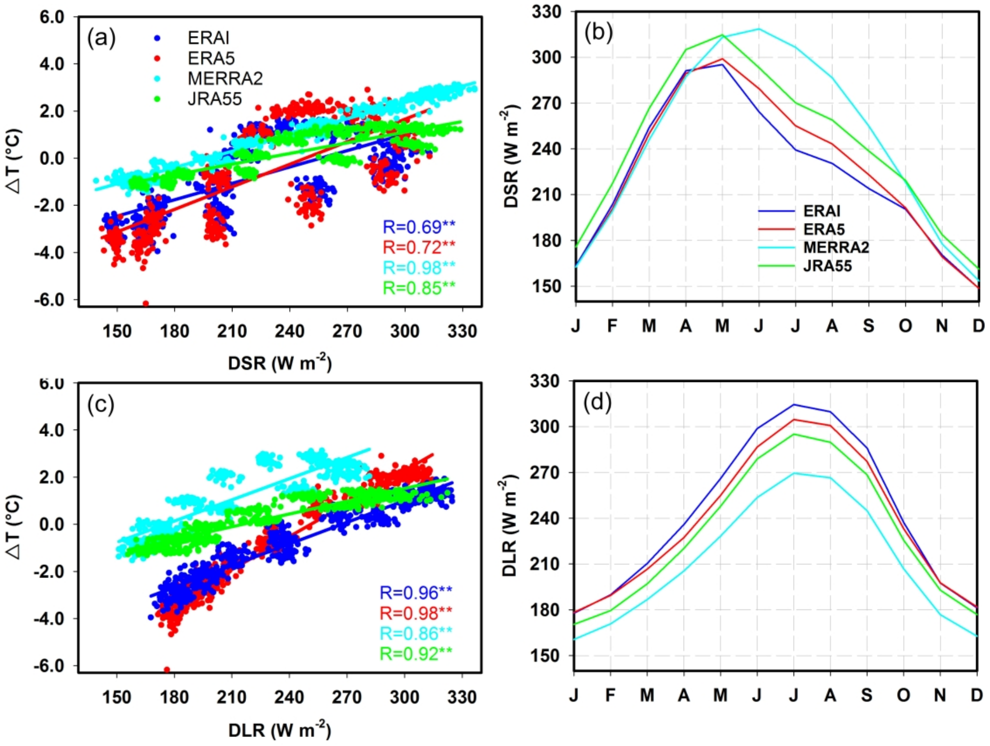

Figure 6 Relationship between monthly ∆T and downward shortwave radiation (DSR), downward longwave radiation (DLR) from four reanalysis data sets and averaged annual cycles of DSR and DLR on the TP.

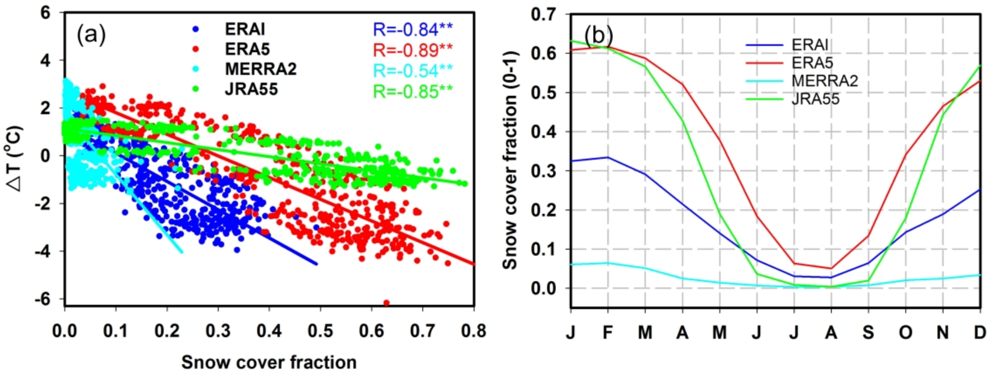

Figure 7 As Figure 6, but for snow cover fraction (SCF).

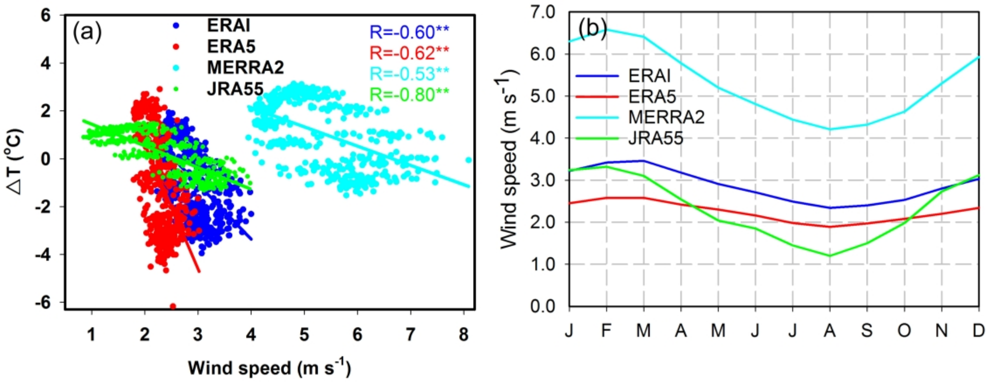

Figure 8 As Figure 6, but for 10-m wind speed (WS).

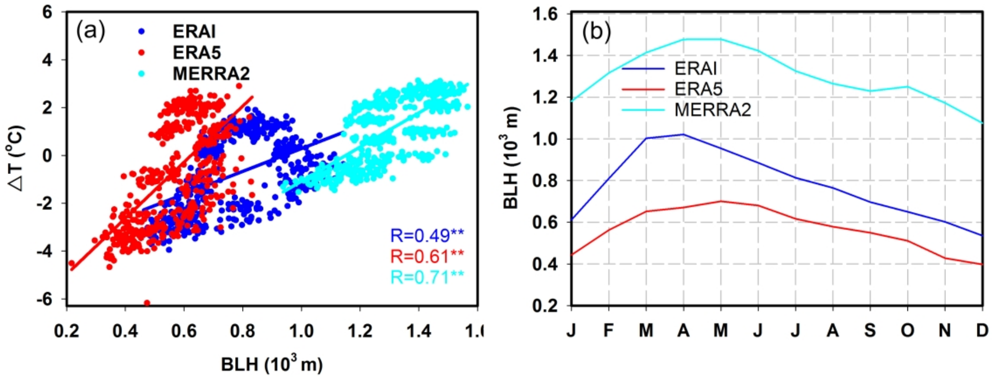

Figure 9 As Figure 6, but for boundary layer height (BLH). BLH is not available in JRA55.